NANO LETTERS
Letter
Cite This: Nano Lett. 2019, 19, 6192−6202
pubs.acs.org/NanoLett

Ultrasensitive Three-Dimensional Orientation Imaging of Single Molecules on Plasmonic Nanohole Arrays Using Second Harmonic Generation

Sushant P. Sahu,[†,⊥] Amirreza Mahigir,[‡,§,⊥] Benjamin Chidester,[∥] Georgios Veronis,[‡,§] and Manas Ranjan Gartia*[,†]

[†]Department of Mechanical and Industrial Engineering, Louisiana State University, Baton Rouge, Louisiana 70803, United States
[‡]School of Electrical Engineering and Computer Science, Louisiana State University, Baton Rouge, Louisiana 70803, United States
[§]Center for Computation and Technology, Louisiana State University, Baton Rouge, Louisiana 70803, United States
[∥]Department of Computational Biology, School of Computer Science, Carnegie Mellon University, Pittsburgh, Pennsylvania 15213, United States

Supporting Information

ABSTRACT: Recently, fluorescence-based super-resolution techniques such as stimulated emission depletion (STED) and stochastic optical reconstruction microscopy (STORM) have been developed to achieve near molecular-scale resolution. However, such a super-resolution technique for nonlinear label-free microscopy based on second harmonic generation (SHG) is lacking. Since SHG is label-free and does not involve real-energy level transitions, fluorescence-based super-resolution techniques such as STED cannot be applied to improve the resolution. In addition, due to the coherent and non-isotropic emission nature of SHG, single-molecule localization techniques based on isotropic emission of fluorescent molecule such as STORM will not be appropriate. Single molecule SHG microscopy is largely hindered due to the very weak nonlinear optical scattering cross sections of SHG scattering processes. Thus, enhancing SHG using plasmonic nanostructures and nanoantennas has recently gained much attention owing to the potential of various nanoscale geometries to tightly confine electromagnetic fields into small volumes. This confinement provides substantial enhancement of electromagnetic field in nanoscale regions of interest, which can significantly boost the nonlinear signal produced by molecules located in the plasmonic hotspots. However, to date, plasmon-enhanced SHG has been primarily applied for the measurement of bulk properties of the materials/molecules, and single molecule SHG imaging along with its orientation information has not been realized yet. Herein, we achieved simultaneous visualization and three-dimensional (3D) orientation imaging of individual rhodamine 6G (R6G) molecules in the presence of plasmonic silver nanohole arrays. SHG and two-photon fluorescence microscopy experiments together with finite-difference time-domain (FDTD) simulations revealed a ∼10^6-fold nonlinear enhancement factor at the hot spots on the plasmonic silver nanohole substrate, enabling detection of single molecules using SHG. The position and 3D orientation of R6G molecules were determined using the template matching algorithm by comparing the experimental data with the calculated dipole emission images. These findings could enable SHG-based single molecule detection and orientation imaging of molecules which could lead to a wide range of applications from nanophotonics to super-resolution SHG imaging of biological cells and tissues.

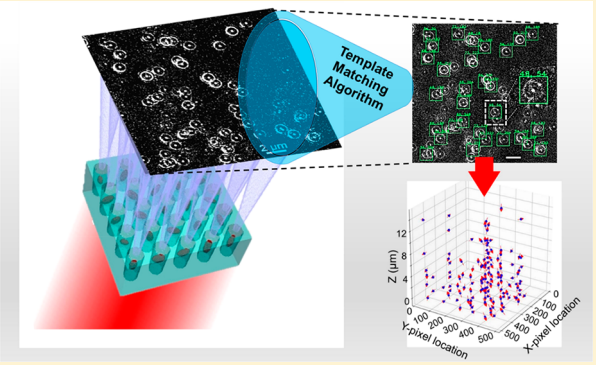

KEYWORDS: *Single molecule imaging, second harmonic generation, orientation, nanohole arrays*

Fluorescence-based super-resolution techniques such as stimulated emission depletion (STED)[1,2] and photoactivated localization microscopy (photoactivated localization microscopy, PALM; fluorescence photoactivation localization microscopy, FPALM, STORM)[3,4] have been developed to achieve near molecular-scale resolution. However, such a super-resolution technique for nonlinear label-free microscopy based on second harmonic generation (SHG) is lacking. Point spread function (PSF) is generally engineered to improve the resolution of a microscopy system. Fluorescence emissions are typically incoherent, and the radiation patterns are isotropic. In contrast, SHG emission is coherent, and radiation patterns are directional in nature.[5,6] Therefore, the super-resolution techniques developed for fluorescence microscopy systems are not readily applicable to nonlinear microscopy systems such as SHG.

Received: June 1, 2019
Revised: August 1, 2019
Published: August 7, 2019

DOI: 10.1021/acs.nanolett.9b02239
Nano Lett. 2019, 19, 6192−6202

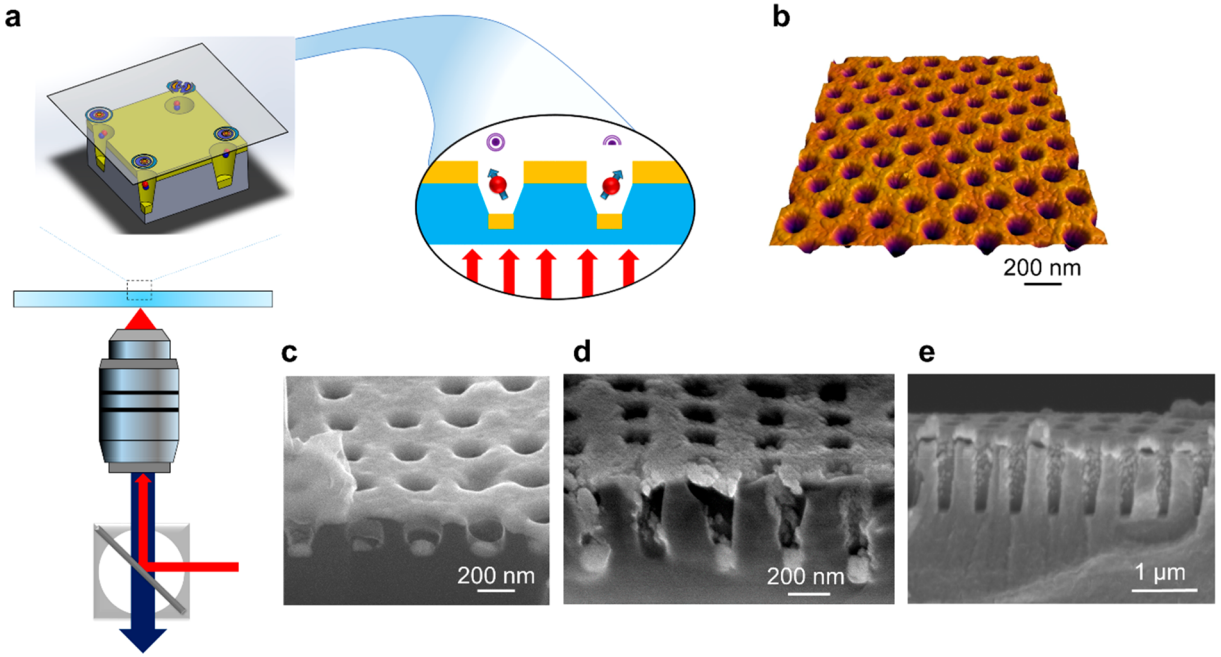

Figure 1. (a) Schematic of the SHG experiments showing the inverted microscopy setup and the position of the sample. The zoomed in image shows the molecule as a dipole emitter within individual silver nanoholes. (b) AFM image of the fabricated structures showing the periodic array of nanoholes. Cross-sectional SEM image of the device showing the device with hole depth of (c) 250 nm, (d) 500 nm, and (e) 1000 nm.

SHG is a nonlinear coherent optical scattering process usually by noncentrosymmetric systems in which two lower energy photons are up-converted to a single photon with exactly double the incident light energy. The SHG yield grows as the square of the fundamental incident field intensity.[7−9] Enhancing SHG from plasmonic nanostructures and nanoantennas has recently received a lot of attention owing to the potential of various nanoscale geometries to tightly confine electromagnetic fields into small volumes and provide substantial field enhancement in nanoscale regions of interest.[8,10−20] The plasmonic resonances from nanostructures have been utilized for a multitude of photonic applications including surface-plasmon enhanced nonlinear emission,[10−19] single molecule detection,[21] surface-enhanced Raman scattering,[22−24] metal-enhanced photoluminescence,[25,26] plasmon-enhanced sensing,[16,17] photocatalysis,[27] and optical manipulation of light.[28,29] Thoughtful design and surface engineering of plasmonic nanostructured arrays are able to produce areas called "hot spots" where the induced electromagnetic field intensity is enhanced by several orders of magnitude which can significantly increase the nonlinear signal produced by a nonlinear material located in plasmonic nanogaps, especially when resonantly pumped.[20] Plasmonic nanostructures resulting in generation of second harmonic light include gold nanostars,[30] silver triangular nanoprisms,[31] holes in metallic films,[32] curved nanorods,[33] split-ring resonators with U-shape,[34] metal-dielectric nanodisks,[35] gold T-dimers,[36] nanocups,[37] chiral G-shaped nanoparticles,[38] chiral helices,[39] L-shaped nanoparticles,[40] and gold nanotips.[41] Previously we have used a nanohole-based plasmonic substrate in the linear optical regime to achieve highly sensitive colorimetric sensing[23,42] and enhancement of Raman scattering of the order of 2×10^5.[24] Here, we operate a nanohole array-based substrate in the nonlinear optical regime and demonstrate highly sensitive single molecule detection and simultaneous three-dimensional (3D) orientation mapping of rhodamine 6G (R6G) molecules using SHG microscopy. Determining the molecular orientation of single molecules is fundamentally important in biophysics to study conformational changes of biomolecules[43] and/or the rotational motion of molecular motors,[44] in the analyses of photophysical processes such as fluorescence resonance energy transfer (FRET) which are governed by orientation of materials,[45] in molecular nanotechnology,[46] biotechnology,[47] and also in catalysis.[48] Previous methods of determining the 3D dipole orientation of single fluorescent molecules include: (i) probing the far-field emission pattern through polarization-resolved microscopy methods that rely on excitation and/or emission with multiple polarizations,[49,50] (ii) observing a dipole radiation pattern in defocused wide-field imaging technique which takes advantage of bright fluorescence properties of dipole emitters as opposed to very weak nonlinear optical cross sections of processes such as SHG,[51] (iii) direct imaging of pupil functions,[52] (iv) double-helix point spread function engineering,[53] and (v) using annular illumination to generate characteristic field distributions.[54] However, similar 3D orientation information with single-molecule resolution has not been obtained using nonlinear microscopy techniques such as SHG.

In this letter, we introduce an ultrasensitive collective plasmon-enhanced SHG microscopy method for simultaneous visualization and 3D orientation imaging of individual R6G molecules using plasmonic silver nanohole arrays. SHG and two-photon fluorescence microscopy experiments together with numerical simulation results suggest several orders of electromagnetic field enhancement at the surface hot spots on the plasmonic nanohole substrate compared to R6G molecules immobilized on a glass substrate, enabling detection of significantly amplified plasmon-enhanced SHG signatures from individual R6G molecules on the plasmonic silver nanohole structure.

Results and Discussion. The schematic of the experimental set up is shown in Figure 1a. The figure shows the excitation beam (red) and the collected emitted SHG light (blue) from the molecule on the plasmonic substrate. For the square nanohole

DOI: 10.1021/acs.nanolett.9b02239
Nano Lett. 2019, 19, 6192−6202

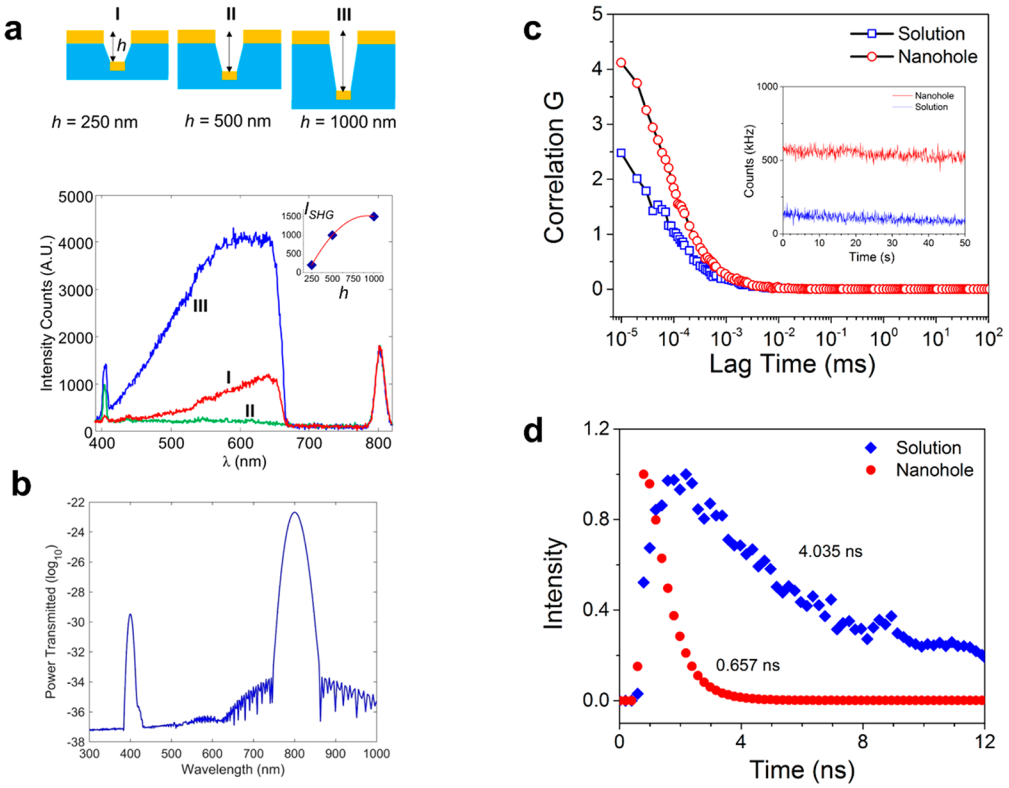

Figure 2. (a) Schematic of the nanohole device with three different hole depths on which SHG experiments were performed. Experimental SHG spectra generated by the nanohole devices with different hole depths. The inset shows the variation of SHG intensity at 400 nm with the hole depths. (b) Calculated transmission coefficient through the nanohole array as a function of wavelength. A high-power excitation plane wave with 800 nm wavelength is used to excite the structure. The second harmonic resonance of the structure is at 400 nm. (c) Fluorescence correlation functions measured for R6G in a solution and on the silver nanohole structure (h = 500 nm). The inset shows the corresponding fluorescence time traces. (d) Fluorescence lifetime analysis of R6G with and without the nanohole structure.

array with a pitch (distance between two holes) of 350 nm, a structure with a size of 1 cm × 1 cm contains about 100 million holes. This provides a unique platform to perform massively parallel single-molecule imaging. The rationale behind the nanohole structure is to restrict only a few molecules (~0.3) within the confocal volume. In addition, this geometry minimizes the background and improves the signal-to-noise (SNR) by preventing the direct excitation of molecules away from the holes due to lower electromagnetic field intensity outside the holes. The nanohole structure was fabricated by nanoimprint lithography (see Materials and Methods). As shown in the AFM image (Figure 1b), the nanoholes are arranged in a square geometry with hole diameter d = 150 nm and pitch p = 350 nm. Large area (1 cm^2) substrates were fabricated with three different hole depths. The diameter and the pitch were kept constant. The depth of the holes h was varied between 250 and 1000 nm. Figure 1c–e shows the cross-sectional scanning electron microscopy (SEM) images of the substrate with three different depths. The AFM image in Figure 1 and additional top-view SEM images (Supporting Information (SI) Figure S1) showed that the designed nanohole arrays exhibit a regular square pattern geometry in terms of their sizes and shapes.

The optical linear resonance spectra of nanohole structures of various geometries and thicknesses have been discussed in detail in our prior studies.[42] Figure 2a shows the measured SHG emission spectra of the device with different nanohole depths of 250, 500, and 1000 nm, under a pulsed laser excitation wavelength of 800 nm. The spectra show the SHG peaks at 400 nm and strong broadband two-photon fluorescence in the range of 425–660 nm. Two photon fluorescence in silver nanostructures is generated due to the transition of electrons from the *d*-band (valence band) to the *sp*-band (conduction band). This emitted broadband luminescence is due to the radiative recombination of electrons and holes after the intraband scattering relaxation of electrons to the Fermi level.[55] The SHG from the silver nanohole structure is possible because of the existence of nonzero χ^2 value (second-order nonlinear susceptibility) at the silver–polymer and silver–air interfaces due to the breaking of symmetry of boundary conditions.[56] As the inset of Figure 2a shows, the SHG and two-photon fluorescence signal intensity of the silver nanohole array increased with increase in the depth of the structure [although the lowest two-photon fluorescence yield was obtained for the nanohole structure with hole depth of 500 nm (Figure 2a)]. It is to be noted that the SHG and two photon fluorescence intensities of the nanohole structures can vary from structure to structure likely due to the inhomogeneous distribution of the apex dimensions of the nanohole array.[57] To better understand the mechanism behind SHG emission on the plasmonic nanohole structure, finite-difference time-domain (FDTD) simulations[58] were performed. In order to obtain the second harmonic resonance of the structure, a high-power laser pulse was used. In our FDTD simulations we use a plane wave at 800 nm wavelength normally incident on the nanohole array which excites the second harmonic resonance of the structure. Figure 2b shows the power transmission coefficient of the structure as a function of wavelength in logarithmic scale. We

DOI: 10.1021/acs.nanolett.9b02239
Nano Lett. 2019, 19, 6192–6202

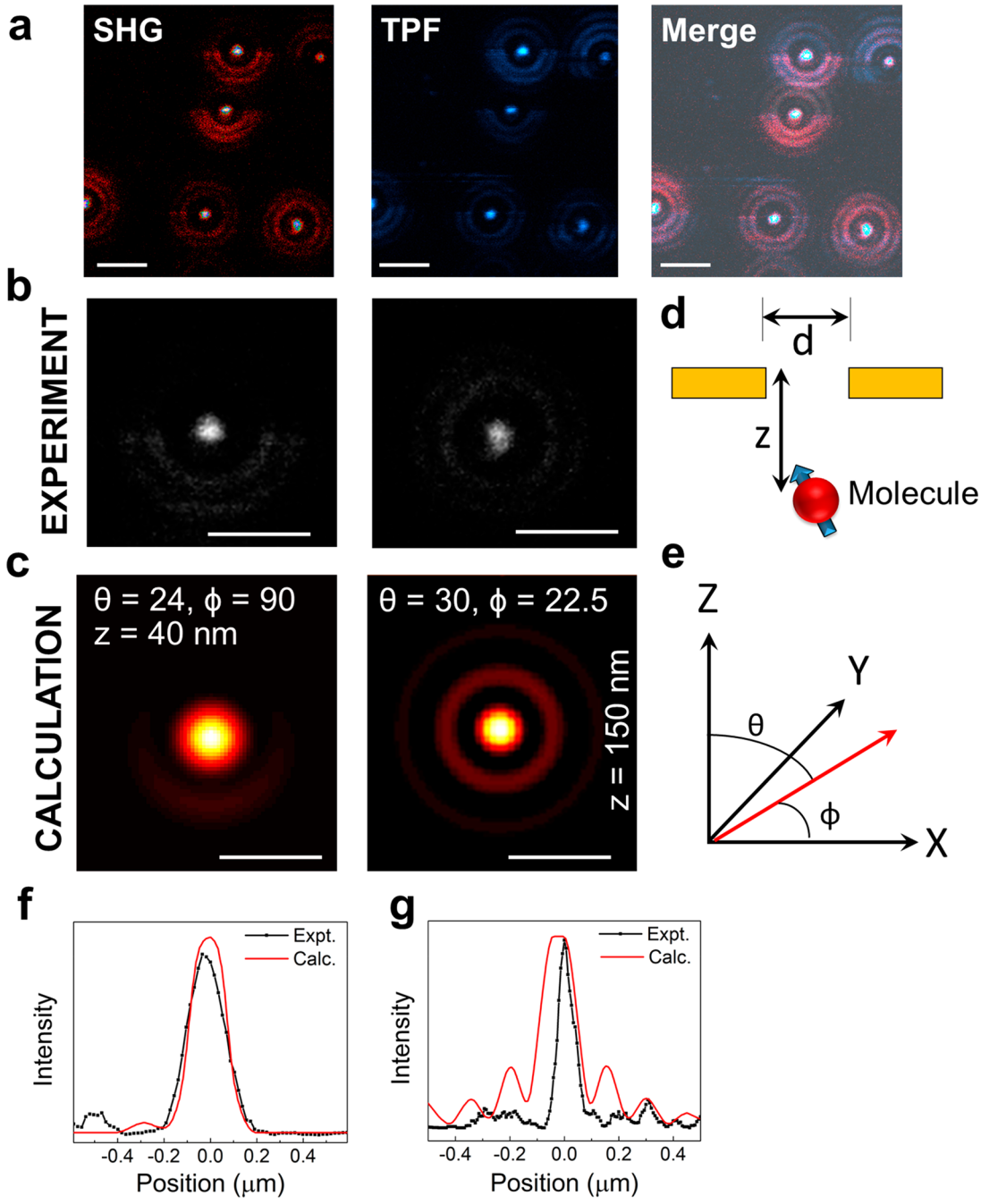

Figure 3. (a) SHG, two-photon fluorescence (TPF), and merged images of single-molecule R6G on the nanohole structure. Representative images of single R6G molecules at depths of z = 40 nm and 150 nm from the (b) experimental data and (c) the corresponding simulation results of the dipole emission patterns through the aperture (nanohole structure). (d, e) Schematic depiction of nanohole aperture, distance of the molecule from the surface, and the coordinate system where the Z is the optical axis, θ is the polar angle measured with respect to Z, and ϕ is the azimuthal angle measured with respect to the Z axis. Comparison of experimental and simulation results shown in Figure 3b,c for two different positions: (f) z = 40 nm and (g) z = 150 nm. The scale bars in all images correspond to 500 nm.

observe that a second resonance appears at the second harmonic wavelength of 400 nm in close agreement with our experimental results (Figure 2a). Due to the low two-photon fluorescence background, a substrate with a nanohole depth of 500 nm was chosen for the subsequent single-molecule SHG imaging experiments.

To demonstrate single-molecule imaging, rhodamine-6G (R6G) dye with a concentration of 0.25 nM was dispersed on the surface of the plasmonic nanohole structure. First, we want to provide experimental proof of the presence of the single molecule within the nanohole at that concentration using fluorescence correlation spectroscopy (FCS).[59] The correlation function in FCS $G(\tau) = \langle F(t)F(t+\tau)\rangle/\langle F(t)\rangle^2$ has an inverse relationship with the number of molecules within the detection volume, where τ is the delay (lag) time. Figure 2c indicates that the number of molecules in the nanohole is smaller compared to the bulk solution based on measurements of their autocorrelation functions. The inset of Figure 2c shows the raw data of photon counts rate on the nanohole and bulk solutions. The nanohole structure exhibits about 5× enhancement compared to

DOI: 10.1021/acs.nanolett.9b02239
Nano Lett. 2019, 19, 6192−6202

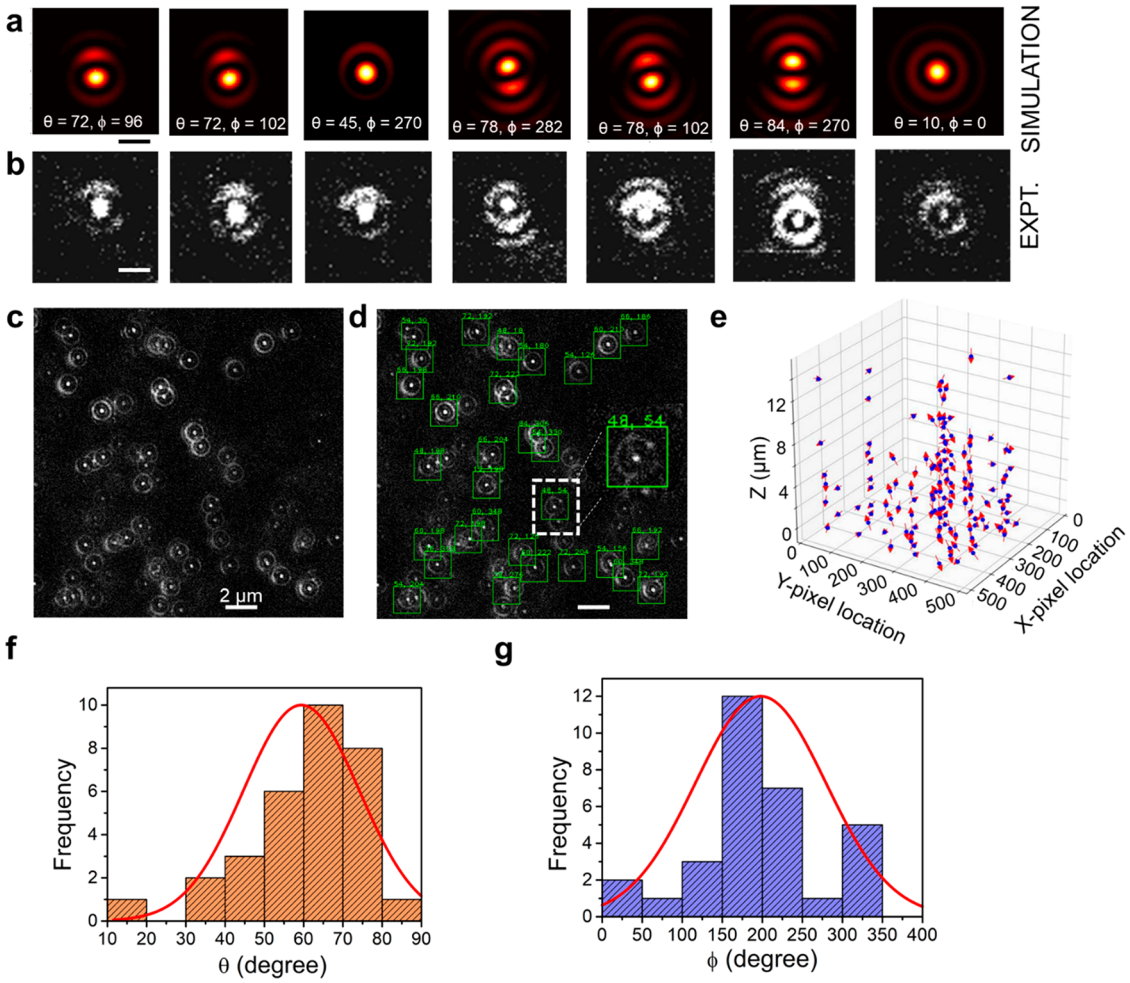

Figure 4. Template matching algorithm to find the orientation of the molecule in 3D. (a) Simulated images at different θ and ϕ at fixed aperture. (b) Examples of corresponding experimental SHG images with matching patterns simulated in (a). The scale bars in (a) and (b) correspond to 500 nm. (c) Representative SHG images of R6G molecules on the nanohole substrate. (d) Values of θ and ϕ indicated in the image obtained by the template matching algorithm for Figure 4c. The scale bars in (c) and (d) corresponds to 2 μm. (e) 3D mapping of single molecule with its orientation predicted by the template matching algorithm. The blue dot represents the position of the molecule, and the resultant angles of θ and ϕ are denoted by the red arrows. Histogram distribution of orientation angles in (f) polar direction, θ, and (g) azimuthal direction, ϕ.

the bulk dye solution. The average number of molecules within the nanohole was calculated by fitting the equation below to the data obtained from fluorescence correlation spectroscopy experiments[59,60]

$$G_0 = 1 + \frac{1}{N}\left(1 - \frac{\langle b\rangle}{\langle i\rangle}\right)^2 (1 + n_T)$$

where $\langle i\rangle$ is the average measured intensity, $\langle b\rangle$ is the background intensity counts, and n_T is the number of molecules in the triplet state, which is 0.35.[60] G_0 is obtained from the function fitted to autocorrelation data for the nanohole and is found to be ~4.76. Using the data, the average number of molecules in the nanohole for this particular concentration was found to be ~0.3 (see SI for the calculations). To get information about the radiative process involved with the enhancement on the nanohole array structure, fluorescence lifetime experiments were performed. Figure 2d compares the lifetime of R6G on the nanohole and in bulk solution. The lifetime in bulk was measured to be 4.035 ns, which agrees well with the literature data.[61] The lifetime was decreased by 6× on the nanohole structure compared to the bulk value. Since the fluorescence lifetime is $\tau = 1/(\Gamma + k_{NR})$, where Γ is the radiative decay rate, and k_{NR} is the nonradiative decay rate, and the quantum yield is $Q = \Gamma/(\Gamma + k_{NR})$, we can write $\Gamma = Q/\tau$, and $k_{NR} = (1/\tau) - \Gamma$. Our experiments showed a decrease in lifetime with an increase in quantum yield (Figure 2c,d). This indicates that the enhancement on the nanohole is mainly driven by an increase in the radiative decay process.[62]

Next, control experiments were performed on the glass substrate without the silver nanohole substrate. Since the field intensity enhancement is low without any plasmonic nanostructure, a 400× higher concentration of R6G is required on glass to get any detectable signal, and such a concentration was employed in our experiments. Both samples (R6G on glass and nanohole structure) showed a two-photon fluorescence in the emission wavelength range of R6G (~550−560 nm) (Figure S5b,d). However, only the nanohole plasmonic structure with R6G showed SHG (Figure S5c). Despite using a 400× higher concentration of R6G (10 μM), the glass substrate did not show any SHG signal (Figure S5a). The samples on glass showed SHG at a R6G concentration of about 11 mM (Figure S7). Also, we did not observe any detectable SHG on smooth Ag and Au metal alone (Figure S6), which is expected because of a

DOI: 10.1021/acs.nanolett.9b02239
Nano Lett. 2019, 19, 6192−6202

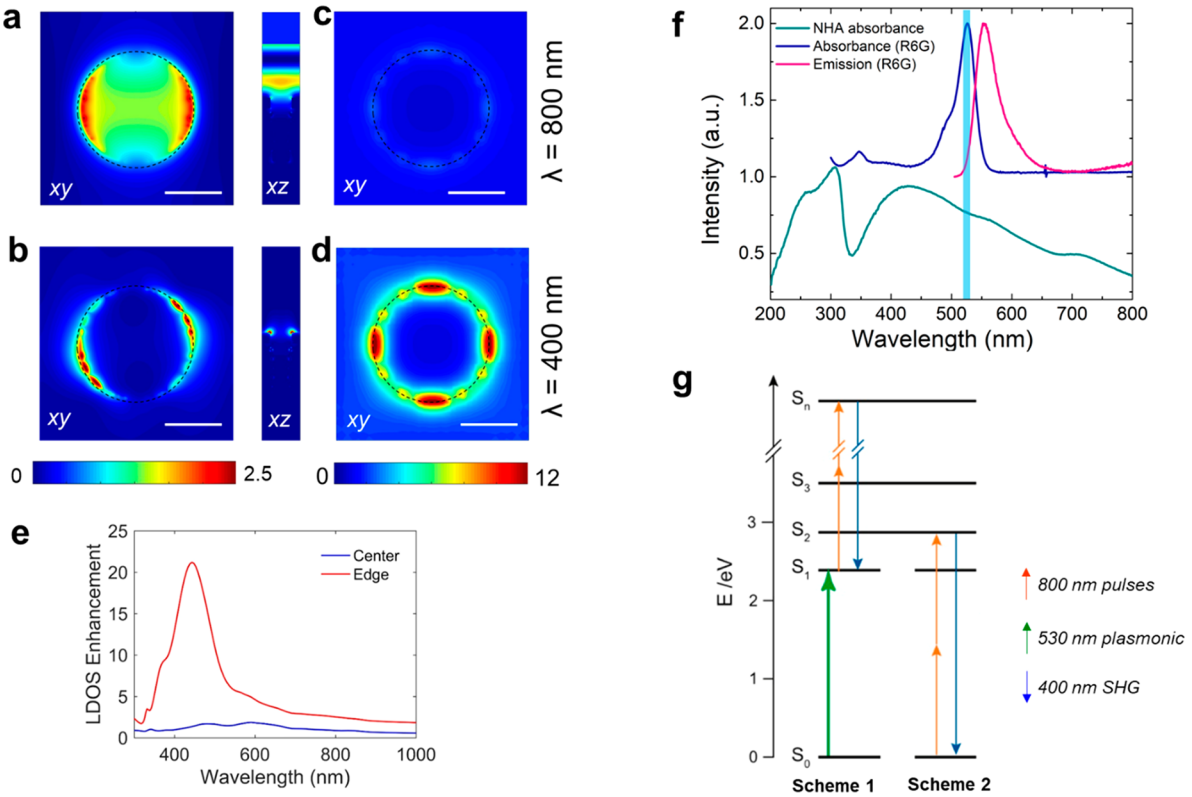

Figure 5. Electric field intensity calculated at (a) λ = 800 nm and plotted in the *xy* plane (top view of the nanohole device). The image on the right shows the electric field distribution in the *xz* plane (side view or along the cross section of the nanohole device) calculated at λ = 800 nm. (b) The corresponding electric field distribution in the *xy* and *xz* planes calculated at λ = 400 nm. Local density of photonic states (LDOS) enhancement map calculated on the surface of the nanohole array at (c) λ = 800 nm and (d) λ = 400 nm. (e) LDOS enhancement variation with wavelength calculated at the center of the nanohole (blue) and at the edges of the nanohole. (f) Absorbance of the nanohole array (NHA) device showing the plasmonic resonance of the structure with h = 1000 nm. The absorption and emission spectra of R6G are also plotted showing the plasmonic−R6G molecule interaction. (g) Jablonski diagram showing the probable energy transitions scheme for the plasmon-enhanced SHG signal generation from single R6G molecules.

centrosymmetric crystal lattice of the smooth continuous metal thin films where SHG is forbidden in bulk due to inversion symmetry. The R6G detection on smooth metal substrate was found to be dependent on the concentration of R6G dye employed in the experiments with an obvious greater sensitivity for detection at higher R6G concentrations particularly in sub-mM concentration range.

Figure 3 presents the single-molecule SHG imaging of R6G within nanoholes, where each molecule has a different orientation. Various patterns were observed with central bright spots with two full or half Airy ring-like structures. It should be noted that the half-ring-like structures are not imaging artifacts, which we verified by changing the imaging speed and pixel dwelling time. Furthermore, these are not due to digital photobleaching since SHG should not show any photobleaching.[63] As seen in Figure 3a, Airy disk emission patterns were visible only for R6G on the nanohole structures and not on the glass substrate (Figure S5a). Interestingly, some of the emission patterns also showed half-Airy disk structures that are attributed to different orientations of R6G molecules on the nanohole substrate. We also note that we did not observe such unique Airy ring-like patterns when imaging the plasmonic silver nanohole structure alone without R6G dye, where the SHG channel shows weakly emissive dots arising from the silver nanostructures on the nanohole device (Figure S8). To find the reason for the unique half-Airy ring patterns in the presence of R6G dye, we calculated the emission pattern of the dipole radiated through the aperture.[49] Here, we modeled the fluorescence dye as a dipole emitter, and the nanohole as an aperture. Such calculations were performed closely resembling the nanohole geometry described at different aperture diameters d, depths of dipole from the aperture z, polar angle θ, pixel size $n \times n$, and azimuthal angle ϕ to generate a library of images (Figures 3c and 4a and SI Figure S9). A total of 72,000 template images were created for the library. Using the template matching algorithm (see Materials and Methods and SI for details), the experimental results were compared with the simulated library images to find the corresponding d, z, θ, and ϕ by finding the best possible match between a given image region and the set of library images. It was found that the half-Airy patterns of the SHG were due to the different orientations of the R6G molecules inside the nanohole. The experiment and the simulation of the dipole emission patterns through the aperture (nanohole device) are matched within our angular uncertainty analyses, indicating that the molecule (Figure 3b, left) has a polar angle $\theta = 24°$ and azimuthal angle $\phi = 90°$ and is situated at 40 nm from the surface, while the molecule (Figure 3b right) is located at 150 nm from the surface having a polar angle of $\theta = 30$ and azimuthal angle of $\phi = 22.5°$ (Figure 3b,c,f,g). Figure 4a shows the various simulated patterns of single molecules with different orientations at various aperture depths. The corresponding identified experimental patterns are shown in Figure 4b. The similarity of the patterns for the experimental and simulated images can be clearly observed, confirming the

DOI: 10.1021/acs.nanolett.9b02239
Nano Lett. 2019, 19, 6192−6202

suitability of the algorithm. Furthermore, electromagnetic simulations of the dipole emission pattern calculated at different polar and azimuthal angles were compared with the z-stack experimental SHG imaging to recover the orientation angles θ, ϕ of the molecule inside the plasmonic nanohole structure. Figure 4c,d shows various SHG emission patterns from R6G molecules on the plasmonic nanoholes in a larger field of view with many individual molecules at a single plane. Figure 4e represents 3D mapping of individual R6G molecules obtained from the z-stack of images. The purpose of Figure 4e was to demonstrate the optical sectioning capability of multiphoton nonlinear SHG microscopy with 3D orientation mapping by imaging through sequential z- slices through collection of a z-stack of images. The locations of the molecules are shown as blue dots, and the resultant vector angles of θ and ϕ are denoted by the red arrows for the 31 molecules imaged. This is the first demonstration of highly sensitive simultaneous visualization and 3D orientation extraction of individual R6G molecules using label-free SHG imaging on plasmonic nanohole arrays. Figure 4f,g shows the histogram distribution of extracted orientation angles θ, ϕ from SHG images. It should be noted that when we include large numbers of molecular images (~150 molecules and see SI Figure S12) in our analysis, the azimuthal angle (ϕ) distribution is relatively flat, which means that molecules can be found with almost equal probability in any ϕ angle ranging from 0° to 360°. The observed SHG emissions results in Figure S12 show that the most probable orientation of molecules in terms of polar angle is at $\theta = 60-70°$, which agrees well with the literature values.[64,65] It should be noted that for unambiguous detection of molecules, the outer rim of the pattern is very helpful. Therefore, for precise analysis of orientation angles, the ideal separation between molecules is determined to be ~1.0−1.5 μm. Figure 4d depicts the fitted experimentally obtained SHG emission patterns using the template matching algorithm to obtain both out-of-plane and in-plane-orientation angles θ, ϕ, demonstrating that emission from single molecules matches the one of dipole emitters. However, we also note that it becomes progressively harder to distinguish patterns with an out-of-plane angle of <30°, especially for images with poor signal-to-noise ratio. The image analysis of Figures 3 and 4 shows that the algorithm performs well for relatively non-overlapping molecular orientation patterns, even with poor signal-to-noise counts. Our analysis showed that, if the polar angle of orientation for the two molecules is between $\theta = 0-30°$, we will likely not be able to resolve it, though we can still produce some estimate. However, our theoretical templates sample the possible values of $\theta = 6°$ and $\phi = 6°$ using the template matching algorithm employed. So, though our theoretical resolution is 6°, in reality, our ability to resolve angles depends highly upon θ.

To understand the mechanism of enhanced surface-sensitive SHG response from individual R6G molecules on plasmonic nanohole arrays, we performed numerical simulations to calculate the field enhancement and local density of states (LDOS) at plasmonic hot spots on silver nanohole arrays. R6G is known to exhibit polarization-sensitive SHG emission, albeit at high sub-mM range of concentrations, in ensemble measurements at a pump laser excitation of 780−800 nm.[66] We calculated the electric field intensity distribution in one unit cell of the nanostructure at both 800 and 400 nm wavelengths (Figure 5a,b). We observe that, while at 800 nm the structure does not have any strong resonances, at 400 nm the electric field is highly intensified at the edges of the nanohole. Molecules adsorbed close to these hot spots on the surface of the structure experience a significant increase in the local fields, which consequently enhances light-matter interactions at the location of these molecules. From Figure 5b, we observe that at 400 nm, we have ~2.5× electromagnetic field enhancement on the edges of the silver nanohole compared to the planar silver surface.

The intensified confinement of the electromagnetic field at the second harmonic resonance wavelength (λ = 400 nm) increases the LDOS at the outer rim of the nanoholes (Figure 5c,d). According to Fermi's golden rule, the increase in the LDOS leads to an increase in the spontaneous emission rate of a dipole as follows:[67,68] $\gamma_{sp=2\omega/3\hbar\epsilon_0|\mu|^2} \int_s \rho(r,\omega) ds$ where $\rho(r,\omega)$ is the LDOS, $\hbar$ is the reduced Planck constant, ϵ_0 is the dielectric permittivity of free space, and μ is the transition dipole moment of the emitter. The LDOS $\rho(r,\omega)$ was calculated using the equation:[67,68] $\rho(r, \omega) = \frac{2\omega}{\pi c^2}\{\hat{n}_p \cdot \mathrm{Im}\{\mathrm{Tr}[\overleftrightarrow{G}(r, r)] \cdot \hat{n}_p\}\}$, where $\hat{n}_p$ is the orientation of the transition dipole of the emitter, $\overleftrightarrow{G}$ is the dyadic Green's function, and c is the speed of light in free space. Here, the function $\overleftrightarrow{G}$ takes in to account the interplay between the dipole of the emitter with its own local electric field. Using the above equation, the LDOS was calculated at the center and at the outer rims of the nanohole at λ = 400 and 800 nm. In the FDTD simulations, an electric dipole emitter was positioned at the center and at the edges of the nanohole, while its vertical location was 2 nm above the surface of the sample. Figure 5e shows the LDOS enhancement at the center of the nanohole (blue) and at the outer rim of the nanohole (red). The LDOS was calculated by averaging the DOS of the dipole emitter over the three polarization directions. We observe that the LDOS is significantly increased at the edges of the nanohole compared to the center. The spatial dependence of the LDOS is shown in Figure 5c,d (λ = 800 nm and 400 nm, respectively). The LDOS, and consequently the spontaneous emission rate from an emitter, increases by more than an order of magnitude (~12×) at the edges of the nanohole at the 400 nm wavelength (Figure 5c−e). Therefore, our experimental and simulation results suggest that the increased confinement of the electromagnetic field at the hot spot locations near the R6G molecules lead to enhancement of SHG emission on our device. Further, the confinement leads to enhanced light absorption and an increase in the LDOS near the location of the R6G molecules, resulting in an enhanced emission rate of R6G at the wavelength of 400 nm. As seen in Figure 5b,d, the excitation electromagnetic field enhancement at 400 nm of ~2.5 on plasmonic hot spots in combination with the emission enhancement of ~12 in LDOS near the edges of the nanohole at 400 nm provides at least 30× total enhancement on the edges of the plasmonic silver nanohole substrate. We do not see any SHG signal originating from R6G at 10 μM concentration on the glass substrate, while on the silver nanohole structure even at very dilute 0.25 nM concentration, we observe SHG emission from single R6G molecules. As the SHG signal is proportional to the number of molecules ($I_{SHG} \propto N\beta$, where N is the number of molecules and β is the hyperpolarizability of the molecule),[69] the magnitude of SHG enhancement factor (EF) on the plasmonic silver nanohole arrays is estimated to be

$$\mathrm{EF} \sim I_{\mathrm{nanohole}} N_{\mathrm{glass}} / I_{\mathrm{glass}} N_{\mathrm{nanohole}} = 1.2 \times 10^6$$

Figure 5g shows the proposed energy level scheme illustrating possible enhancement of the SHG signal from R6G molecules through two different mechanisms denoted as Schemes 1 and 2. Scheme 2 shows the direct generation of SHG photons from

DOI: 10.1021/acs.nanolett.9b02239
Nano Lett. 2019, 19, 6192−6202

R6G. Under an 800 nm pulsed laser excitation source, R6G absorbs two photons to undergo an $S_0 \rightarrow S_2$ transition. When R6G relaxes to its ground state, it will emit the SHG photon at 400 nm due to $S_2 \rightarrow S_0$ transition. However, this transition process is weak, as it requires R6G concentrations above 1 mM (Figure S7). We believe the more dominant SHG emission pathway is likely arising through the configuration of Scheme 1. Therein, broad two photon fluorescence and plasmonic generation of photons at 530 nm from the silver nanohole array provide the pump excitation to populate the singlet state (S_1) of R6G (Figure 5g). Finally, the two-photon absorption generates the SHG signal with a $S_n \leftarrow S_1$ transition followed by a $S_1 \leftarrow S_n$ SHG transition of the R6G molecule under 800 nm pulsed laser excitation. A similar mechanistic framework has been demonstrated for SHG emission in R6G through ensemble measurements.[66]

In summary, we demonstrate a unique SHG microscopy method for ultrasensitive collective plasmon-enhanced SHG to achieve simultaneous visualization and 3D orientation imaging of individual R6G molecules using plasmonic silver nanohole arrays. These findings can be extended to detect and perform orientation imaging of single molecules in applications ranging from nanophotonics to complex biological systems.

Materials and Methods. *Sample Fabrication.* Nanoimprint lithography method was utilized to prepare the nanohole photonic structures.[24,42] Briefly, UV-curable polymer (10 μL) was dropped on a silica master mold (pitch = 350 nm) with nanopillar structure. After curing with a UV flood system with a power density of 105 mW/cm^2, mirror images of the master mold structures were transferred to the supporting PET film to obtain nanohole array structures. Finally, 90 nm of Ag was deposited on the nanohole array PET film for the plasmonic devices.

Experimental Setup and Measurement of SHG Signals. The silver nanohole array plasmonic device dispersed with aqueous R6G (concentration ~0.25 nM) was excited with a Ti-sapphire laser (f = 80 MHz, w_{pulse} = 100 fs, λ_{pump} = 800 nm) (Figure S10) using a 100× objective with numerical aperture of 1.4. The emitted light from the sample was separated by band-pass filters using the spectrometer at 380−400 nm for the SHG signal and 550−650 nm for the two-photon fluorescence signals. The average power at the sample was 10 mW. The obtained single-molecule images were analyzed using a template matching algorithm described below to determine the molecular orientation in each image frame. The resolution of imaging system for SHG images was measured using a 100 nm gold nanoparticle and found to be 670 nm (Figure S11).

Template Matching Algorithm. To determine the depth and orientation of each molecule in the image and compare them to the simulated library of images, we employed a template matching algorithm[70−72] using the normalized cross correlation coefficient as a similarity measure. We first generate a set of templates $\{T_{\{\theta,\phi,z,s\}}(x,y)\}$ that uniformly samples the space of possible parameters of angles (θ and ϕ), scale in number of pixels (s), and depth (z) of the radiation pattern of a molecule/nanoparticle for the given wavelength of the experiment. We iterate over the experimentally generated image with each template, comparing each region in the image to the template using a MATLAB implementation of template matching, and the normalized cross correlation coefficient (NCCC) is given by $\mathrm{NCCC}_T(x, y) = \frac{\sum_{u,v} T(u,v) I(x+u, y+v)}{\sqrt{\sum_{u,v} T^2(u,v) \sum_{u,v} I^2(x+u, y+v)}}$ for each pixel location (x, y), where I is the acquired image and (u, v) are pixel locations in the template. This process yields a score for each template at each pixel location. The maximum score at each pixel is thresholded to remove weak matches which are not likely to correspond to the location of a molecule, producing a binary mask of candidate locations $M(x, y) = \mathrm{I}\left[\max_T \{\mathrm{NCCC}_T(x, y)\} > \tau_{\mathrm{NCCC}}\right]$, where I is the indicator function. Regarding computational time required for the template matching algorithm, typically running the algorithm for one 512 × 512-pixel image for given values of z, aperture, and s (so we are only looking for θ and ϕ) requires ~10−20 s. From there, the time scales linearly in z, aperture, and s.

Quantitative Assessment of Template Matching Algorithm. Theoretically, the only templates that are identical are those for which the vertical/axial angle, θ, is 0. In this case, the imaged pattern will be isotropic, and therefore, changing ϕ (azimuthal angle), which merely rotates the pattern about its center, will not result in any change. For any angle of $\theta > 0$, this will not be the case. However, although the templates will not be exactly the same, the difference may be small, especially for smaller angles of θ.

Figure S13a shows the plots of the NCCC between templates. Recall from above that NCCC ranges from 0−1, with 1 being a perfect match. The first plot shows the pairwise difference between two templates with the same angle θ, varied between 0−90° (corresponding to the column index), but differing values of ϕ (corresponding to row index). For one template, ϕ was held to 0°, while for the other, the angle ϕ was varied from 0 to 360° (corresponding to the row index). We can see that, for values of $\theta < 30°$, changing ϕ, or rotating the template, results in a negligible drop in NCCC. However, for values of $\theta > 30°$, rotation of ϕ results in an increasingly larger drop in NCCC. When θ is nearly 90°, the imaged pattern becomes symmetric to rotations of 180°, which explains the increase in NCCC to 1 for $\phi = 180°$ and $\theta = 90°$. Figure S13b shows the uniqueness of the templates by varying the angle θ and keeping the angle ϕ constant. Along the diagonal, the value of NCCC is 1, since θ is the same for both templates. We can see that, as θ increases beyond a threshold value ($\theta \sim 30°$), the templates become increasingly distinct from each other. However, for $\theta < 30°$, the generated templates are not clearly distinct from each other (NCCC values close to 1). This leads to poor resolution in resolving angles for $\theta < 30°$. On the other hand, when $\theta > 30°$, the angular resolution for resolving the orientation of the molecule is ~6°.

Fluorescence Correlation Spectroscopy. FCS measurements of R6G were conducted on Alba FCS instruments (ISS, USA) based on a Nikon inverted confocal microscope equipped with 470 nm diode laser as a single photon excitation source. Fluorescence intensity fluctuations were detected with an avalanche photodidode detector. All FCS data acquisition and fluorescence intensity temporal fluctuations were analyzed using the VistaVision software package from ISS.

Numerical Simulations. Calculation of the Nonlinear Transmission Coefficient. Lumerical finite difference time domain (FDTD) package was used for the simulations. The refractive indices of silver and titanium were obtained from CRC data, and the refractive index of the polymer was 1.56. The mesh size was 2 nm throughout the simulation domain. Periodic boundary conditions were used in the x and y directions, and perfectly matched layers (PMLs) were used in the z direction. A

DOI: 10.1021/acs.nanolett.9b02239
Nano Lett. 2019, 19, 6192−6202

high-power plane-wave was used to excite the nanostructure as the pump signal (normally incident from top) at 800 nm wavelength. The polarization of the excitation field was along the x direction. The transmitted power was collected using a plane frequency-domain field monitor which was placed below the nanohole array. The spectra were obtained through Fourier transform of the recorded electric fields.

Calculation of the Local Density of States. A simulation domain including several periods of the structure was used to calculate the LDOS. PML boundary conditions were utilized in x, y, and z directions. The mesh size was 1 nm in the vicinity of the surface of the nanostructure and 5 nm in other areas. An electric dipole emitter was positioned at the center and at the edges of the nanohole. Its vertical location was at $z = 2$ nm. For each point (either at the center or at the edge of the nanohole) and for each orientation of the dipole emitter (i.e., x, y, and z), we calculated the Green's function, which is the electric field at r generated by a dipole emitter located at r_0, and used it to obtain the LDOS.

■ ASSOCIATED CONTENT

Supporting Information

The Supporting Information is available free of charge on the ACS Publications website at DOI: 10.1021/acs.nanolett.9b02239.

SEM images of nanohole arrays, optimum power calculation for the FCS experiment; calculating the confocal volume; detailed calculation of number of molecules within a single nanohole; comparison of SHG and two photon fluorescence microscopy on glass, smooth metal, and nanohole array; template library for typical dipole oriented at certain angles; schematic of the experimental set up; PSF of gold nanoparticle, histogram distribution of orientation angles, and quantitative proof of template matching algorithm (PDF)

■ AUTHOR INFORMATION

Corresponding Author

*E-mail: mgartia@lsu.edu. Phone: +1-225-578-5900.

ORCID

Manas Ranjan Gartia: 0000-0001-6243-6780

Author Contributions

⊥S.P.S. and A.M. contributed equally. M.R.G. conceived and designed the experiments. S.P.S. performed the experiments. A.M. performed the FDTD simulations. B.C. wrote the template matching algorithm. M.R.G., S.P.S., B.C., and A.M. analyzed the data and wrote the manuscript. G.V. supervised the FDTD analysis. All the authors provided input on the manuscript.

Notes

The authors declare no competing financial interest.

■ ACKNOWLEDGMENTS

M.R.G. acknowledges LSU start-up fund and Louisiana Board of Regents Support Fund (RCS award contract number: LEQSF(2017-20)-RD-A-04). G.V. acknowledges support from NSF (award number 1254934). SEM images were taken at LSU's Shared Instrumentation Facility (SIF). SHG experiments were performed at Pennington Biomedical Research Center. We thank Drs. David Burk, Logan Liu, and Mayandi Sivaguru for useful discussions.

■ REFERENCES

(1) Hell, S. W.; Wichmann, J. Breaking the diffraction resolution limit by stimulated emission: stimulated-emission-depletion fluorescence microscopy. *Opt. Lett.* **1994**, *19*, 780−782.

(2) Vicidomini, G.; Bianchini, P.; Diaspro, A. STED super-resolved microscopy. *Nat. Methods* **2018**, *15*, 173−182.

(3) Betzig, E.; Patterson, G. H.; Sougrat, R.; Lindwasser, O. W.; Olenych, S.; Bonifacino, J. S.; Davidson, M. W.; Lippincott-Schwartz, J.; Hess, H. F. Imaging intracellular fluorescent proteins at nanometer resolution. *Science* **2006**, *313*, 1642−1645.

(4) Rust, M. J.; Bates, M.; Zhuang, X. Sub-diffraction-limit imaging by stochastic optical reconstruction microscopy (STORM). *Nat. Methods* **2006**, *3*, 793−796.

(5) Saleh, B. E.; Teich, M. C. *Fundamentals of Photonics*; John Wiley & Sons. Inc.: Hoboken, NJ, 1991.

(6) Terakawa, M.; Nedyalkov, N. N. Near-field optics for nano-processing. *Adv. Opt. Technol.* **2016**, *5*, 17−28.

(7) Kauranen, M.; Zayats, A. V. Nonlinear plasmonics. *Nat. Photonics* **2012**, *6*, 737−748.

(8) Butet, J.; Brevet, P.-F.; Martin, O. J. Optical second harmonic generation in plasmonic nanostructures: from fundamental principles to advanced applications. *ACS Nano* **2015**, *9*, 10545−10562.

(9) Tran, R. J.; Sly, K. L.; Conboy, J. C. Applications of surface second harmonic generation in biological sensing. *Annu. Rev. Anal. Chem.* **2017**, *10*, 387−414.

(10) Kim, M.-K.; Sim, H.; Yoon, S. J.; Gong, S.-H.; Ahn, C. W.; Cho, Y.-H.; Lee, Y.-H. Squeezing photons into a point-like space. *Nano Lett.* **2015**, *15*, 4102−4107.

(11) Grinblat, G.; Rahmani, M.; Cortés, E.; Caldarola, M.; Comedi, D.; Maier, S. A.; Bragas, A. V. High-efficiency second harmonic generation from a single hybrid ZnO nanowire/Au plasmonic nano-oligomer. *Nano Lett.* **2014**, *14*, 6660−6665.

(12) Liu, X.; Zhang, Q.; Chong, W. K.; Yip, J. N.; Wen, X.; Li, Z.; Wei, F.; Yu, G.; Xiong, Q.; Sum, T. C. Cooperative enhancement of second-harmonic generation from a single CdS nanobelt-hybrid plasmonic structure. *ACS Nano* **2015**, *9*, 5018−5026.

(13) Timpu, F.; Hendricks, N. R.; Petrov, M.; Ni, S.; Renaut, C.; Wolf, H.; Isa, L.; Kivshar, Y.; Grange, R. Enhanced second-harmonic generation from sequential capillarity-assisted particle assembly of hybrid nanodimers. *Nano Lett.* **2017**, *17*, 5381−5388.

(14) Aouani, H.; Rahmani, M.; Navarro-Cía, M.; Maier, S. A. Third-harmonic-upconversion enhancement from a single semiconductor nanoparticle coupled to a plasmonic antenna. *Nat. Nanotechnol.* **2014**, *9*, 290−294.

(15) Metzger, B.; Hentschel, M.; Schumacher, T.; Lippitz, M.; Ye, X.; Murray, C. B.; Knabe, B.; Buse, K.; Giessen, H. Doubling the efficiency of third harmonic generation by positioning ITO nanocrystals into the hot-spot of plasmonic gap-antennas. *Nano Lett.* **2014**, *14*, 2867−2872.

(16) Shen, S.; Meng, L.; Zhang, Y.; Han, J.; Ma, Z.; Hu, S.; He, Y.; Li, J.; Ren, B.; Shih, T.-M.; et al. Plasmon-enhanced second-harmonic generation nanorulers with ultrahigh sensitivities. *Nano Lett.* **2015**, *15*, 6716−6721.

(17) Ghirardini, L.; Baudrion, A.-L.; Monticelli, M.; Petti, D.; Biagioni, P.; Duò, L.; Pellegrini, G.; Adam, P.-M.; Finazzi, M.; Celebrano, M. Plasmon-enhanced second harmonic sensing. *J. Phys. Chem. C* **2018**, *122*, 11475−11481.

(18) Thyagarajan, K.; Rivier, S.; Lovera, A.; Martin, O. J. Enhanced second-harmonic generation from double resonant plasmonic antennae. *Opt. Express* **2012**, *20*, 12860−12865.

(19) Celebrano, M.; Wu, X.; Baselli, M.; Großmann, S.; Biagioni, P.; Locatelli, A.; De Angelis, C.; Cerullo, G.; Osellame, R.; Hecht, B.; et al. Mode matching in multiresonant plasmonic nanoantennas for enhanced second harmonic generation. *Nat. Nanotechnol.* **2015**, *10*, 412−417.

(20) Muehlschlegel, P.; Eisler, H.-J.; Martin, O. J.; Hecht, B.; Pohl, D. Resonant optical antennas. *Science* **2005**, *308*, 1607−1609.

(21) Ament, I.; Prasad, J.; Henkel, A.; Schmachtel, S.; Sonnichsen, C. Single unlabeled protein detection on individual plasmonic nanoparticles. *Nano Lett.* **2012**, *12*, 1092−1095.

DOI: 10.1021/acs.nanolett.9b02239
Nano Lett. 2019, 19, 6192−6202

(22) Zhang, R.; Zhang, Y.; Dong, Z.; Jiang, S.; Zhang, C.; Chen, L.; Zhang, L.; Liao, Y.; Aizpurua, J.; Luo, Y.; Yang, J. L.; Hou, J. G. Chemical mapping of a single molecule by plasmon-enhanced Raman scattering. *Nature* **2013**, *498*, 82−86.
(23) Chang, T. W.; Wang, X.; Hsiao, A.; Xu, Z.; Lin, G.; Gartia, M. R.; Liu, X.; Liu, G. L. Bifunctional Nano Lycurgus Cup Array Plasmonic Sensor for Colorimetric Sensing and Surface-Enhanced Raman Spectroscopy. *Adv. Opt. Mater.* **2015**, *3*, 1397−1404.
(24) Mahigir, A.; Chang, T.-W.; Behnam, A.; Liu, G. L.; Gartia, M. R.; Veronis, G. Plasmonic nanohole array for enhancing the SERS signal of a single layer of graphene in water. *Sci. Rep.* **2017**, *7*, 14044.
(25) Fu, B.; Flynn, J. D.; Isaacoff, B. P.; Rowland, D. J.; Biteen, J. S. Super-resolving the distance-dependent plasmon-enhanced fluorescence of single dye and fluorescent protein molecules. *J. Phys. Chem. C* **2015**, *119*, 19350−19358.
(26) Li, J.-F.; Li, C.-Y.; Aroca, R. F. Plasmon-enhanced fluorescence spectroscopy. *Chem. Soc. Rev.* **2017**, *46*, 3962−3979.
(27) Hou, W.; Cronin, S. B. A review of surface plasmon resonance-enhanced photocatalysis. *Adv. Funct. Mater.* **2013**, *23*, 1612−1619.
(28) Maragò, O. M.; Jones, P. H.; Gucciardi, P. G.; Volpe, G.; Ferrari, A. C. Optical trapping and manipulation of nanostructures. *Nat. Nanotechnol.* **2013**, *8*, 807−819.
(29) Roxworthy, B. J.; Ko, K. D.; Kumar, A.; Fung, K. H.; Chow, E. K.; Liu, G. L.; Fang, N. X.; Toussaint, K. C., Jr Application of plasmonic bowtie nanoantenna arrays for optical trapping, stacking, and sorting. *Nano Lett.* **2012**, *12*, 796−801.
(30) Senapati, D.; Singh, A. K.; Khan, S. A.; Senapati, T.; Ray, P. C. Probing real time gold nanostar formation process using two-photon scattering spectroscopy. *Chem. Phys. Lett.* **2011**, *504*, 46−51.
(31) Singh, A. K.; Senapati, D.; Neely, A.; Kolawole, G.; Hawker, C.; Ray, P. C. Nonlinear optical properties of triangular silver nanomaterials. *Chem. Phys. Lett.* **2009**, *481*, 94−98.
(32) Schön, P.; Bonod, N.; Devaux, E.; Wenger, J.; Rigneault, H.; Ebbesen, T. W.; Brasselet, S. Enhanced second-harmonic generation from individual metallic nanoapertures. *Opt. Lett.* **2010**, *35*, 4063−4065.
(33) Belardini, A.; Larciprete, M. C.; Centini, M.; Fazio, E.; Sibilia, C.; Chiappe, D.; Martella, C.; Toma, A.; Giordano, M.; Buatier de Mongeot, F. B. Circular dichroism in the optical second-harmonic emission of curved gold metal nanowires. *Phys. Rev. Lett.* **2011**, *107*, 257401.
(34) Linden, S.; Niesler, F.; Förstner, J.; Grynko, Y.; Meier, T.; Wegener, M. Collective effects in second-harmonic generation from split-ring-resonator arrays. *Phys. Rev. Lett.* **2012**, *109*, 015502.
(35) Kruk, S.; Weismann, M.; Bykov, A. Y.; Mamonov, E. A.; Kolmychek, I. A.; Murzina, T.; Panoiu, N. C.; Neshev, D. N.; Kivshar, Y. S. Enhanced magnetic second-harmonic generation from resonant metasurfaces. *ACS Photonics* **2015**, *2*, 1007−1012.
(36) Canfield, B. K.; Husu, H.; Laukkanen, J.; Bai, B.; Kuittinen, M.; Turunen, J.; Kauranen, M. Local field asymmetry drives second-harmonic generation in noncentrosymmetric nanodimers. *Nano Lett.* **2007**, *7*, 1251−1255.
(37) Zhang, Y.; Grady, N. K.; Ayala-Orozco, C.; Halas, N. J. Three-dimensional nanostructures as highly efficient generators of second harmonic light. *Nano Lett.* **2011**, *11*, 5519−5523.
(38) Valev, V.; Silhanek, A.; Verellen, N.; Gillijns, W.; Van Dorpe, P.; Aktsipetrov, O.; Vandenbosch, G.; Moshchalkov, V.; Verbiest, T. Asymmetric optical second-harmonic generation from chiral G-shaped gold nanostructures. *Phys. Rev. Lett.* **2010**, *104*, 127401.
(39) Valev, V.; Clercq, B.; Zheng, X.; Denkova, D.; Osley, E.; Vandendriessche, S.; Silhanek, A.; Volskiy, V.; Warburton, P.; Vandenbosch, G.; et al. The role of chiral local field enhancements below the resolution limit of Second Harmonic Generation microscopy. *Opt. Express* **2012**, *20*, 256−264.
(40) Kujala, S.; Canfield, B. K.; Kauranen, M.; Svirko, Y.; Turunen, J. Multipolar analysis of second-harmonic radiation from gold nanoparticles. *Opt. Express* **2008**, *16*, 17196−17208.
(41) Reichenbach, P.; Horneber, A.; Gollmer, D. A.; Hille, A.; Mihaljevic, J.; Schäfer, C.; Kern, D. P.; Meixner, A. J.; Zhang, D.; Fleischer, M.; et al. Nonlinear optical point light sources through field enhancement at metallic nanocones. *Opt. Express* **2014**, *22*, 15484−15501.
(42) Gartia, M. R.; Hsiao, A.; Pokhriyal, A.; Seo, S.; Kulsharova, G.; Cunningham, B. T.; Bond, T. C.; Liu, G. L. Colorimetric plasmon resonance imaging using nano lycurgus cup arrays. *Adv. Opt. Mater.* **2013**, *1*, 68−76.
(43) Forkey, J. N.; Quinlan, M. E.; Shaw, M. A.; Corrie, J. E.; Goldman, Y. E. Three-dimensional structural dynamics of myosin V by single-molecule fluorescence polarization. *Nature* **2003**, *422*, 399−404.
(44) Toprak, E.; Enderlein, J.; Syed, S.; McKinney, S. A.; Petschek, R. G.; Ha, T.; Goldman, Y. E.; Selvin, P. R. Defocused orientation and position imaging (DOPI) of myosin V. *Proc. Natl. Acad. Sci. U. S. A.* **2006**, *103*, 6495−6499.
(45) Ha, T.; Enderle, T.; Ogletree, D.; Chemla, D. S.; Selvin, P. R.; Weiss, S. Probing the interaction between two single molecules: fluorescence resonance energy transfer between a single donor and a single acceptor. *Proc. Natl. Acad. Sci. U. S. A.* **1996**, *93*, 6264−6268.
(46) Eisenthal, K. B. Second harmonic spectroscopy of aqueous nano- and microparticle interfaces. *Chem. Rev.* **2006**, *106*, 1462−1477.
(47) Peterman, E. J.; Sosa, H.; Moerner, W. Single-molecule fluorescence spectroscopy and microscopy of biomolecular motors. *Annu. Rev. Phys. Chem.* **2004**, *55*, 79−96.
(48) Andoy, N. M.; Zhou, X.; Choudhary, E.; Shen, H.; Liu, G.; Chen, P. Single-molecule catalysis mapping quantifies site-specific activity and uncovers radial activity gradient on single 2D nanocrystals. *J. Am. Chem. Soc.* **2013**, *135*, 1845−1852.
(49) Ishitobi, H.; Nakamura, I.; Hayazawa, N.; Sekkat, Z.; Kawata, S. Orientational imaging of single molecules by using azimuthal and radial polarizations. *J. Phys. Chem. B* **2010**, *114*, 2565−2571.
(50) Ha, T.; Laurence, T. A.; Chemla, D. S.; Weiss, S. Polarization spectroscopy of single fluorescent molecules. *J. Phys. Chem. B* **1999**, *103*, 6839−6850.
(51) Patra, D.; Gregor, I.; Enderlein, J. Image analysis of defocused single-molecule images for three-dimensional molecule orientation studies. *J. Phys. Chem. A* **2004**, *108*, 6836−6841.
(52) Lieb, M. A.; Zavislan, J. M.; Novotny, L. Single-molecule orientations determined by direct emission pattern imaging. *J. Opt. Soc. Am. B* **2004**, *21*, 1210−1215.
(53) Backlund, M. P.; Lew, M. D.; Backer, A. S.; Sahl, S. J.; Grover, G.; Agrawal, A.; Piestun, R.; Moerner, W. Simultaneous, accurate measurement of the 3D position and orientation of single molecules. *Proc. Natl. Acad. Sci. U. S. A.* **2012**, *109*, 19087−19092.
(54) Sick, B.; Hecht, B.; Novotny, L. Orientational imaging of single molecules by annular illumination. *Phys. Rev. Lett.* **2000**, *85*, 4482−4485.
(55) Han, F.; Guan, Z.; Tan, T. S.; Xu, Q.-H. Size-dependent two-photon excitation photoluminescence enhancement in coupled noble-metal nanoparticles. *ACS Appl. Mater. Interfaces* **2012**, *4*, 4746−4751.
(56) Zhou, R.; Lu, H.; Liu, X.; Gong, Y.; Mao, D. Second-harmonic generation from a periodic array of noncentrosymmetric nanoholes. *J. Opt. Soc. Am. B* **2010**, *27*, 2405−2409.
(57) Hou, R.; Shynkar, V.; Lafargue, C.; Kolkowski, R.; Zyss, J.; Lagugné-Labarthet, F. Second harmonic generation from gold meta-molecules with three-fold symmetry. *Phys. Chem. Chem. Phys.* **2016**, *18*, 7956−7965.
(58) Taflove, A.; Hagness, S. C. *Computational Electrodynamics: The Finite-Difference Time-Domain Method*, 2nd ed.; Artech House: Norwood, MA, 2000.
(59) Punj, D.; Mivelle, M.; Moparthi, S. B.; Van Zanten, T. S.; Rigneault, H.; Van Hulst, N. F.; García-Parajó, M. F.; Wenger, J. A plasmonic 'antenna-in-box'platform for enhanced single-molecule analysis at micromolar concentrations. *Nat. Nanotechnol.* **2013**, *8*, 512−516.
(60) Rigneault, H.; Capoulade, J.; Dintinger, J.; Wenger, J.; Bonod, N.; Popov, E.; Ebbesen, T. W.; Lenne, P.-F. Enhancement of single-molecule fluorescence detection in subwavelength apertures. *Phys. Rev. Lett.* **2005**, *95*, 117401.

DOI: 10.1021/acs.nanolett.9b02239
Nano Lett. 2019, 19, 6192−6202

(61) Magde, D.; Wong, R.; Seybold, P. G. Fluorescence Quantum Yields and Their Relation to Lifetimes of Rhodamine 6G and Fluorescein in Nine Solvents: Improved Absolute Standards for Quantum Yields. *Photochem. Photobiol.* **2002**, *75*, 327−334.
(62) Gartia, M. R.; Eichorst, J. P.; Clegg, R. M.; Logan Liu, G. Lifetime imaging of radiative and non-radiative fluorescence decays on nanoplasmonic surface. *Appl. Phys. Lett.* **2012**, *101*, 023118.
(63) Pantazis, P.; Maloney, J.; Wu, D.; Fraser, S. E. Second harmonic generating (SHG) nanoprobes for in vivo imaging. *Proc. Natl. Acad. Sci. U. S. A.* **2010**, *107*, 14535−14540.
(64) Turley, H. K.; Hu, Z.; Jensen, L.; Camden, J. P. Surface-Enhanced Resonance Hyper-Raman Scattering Elucidates the Molecular Orientation of Rhodamine 6G on Silver Colloids. *J. Phys. Chem. Lett.* **2017**, *8*, 1819−1823.
(65) Kikteva, T.; Star, D.; Zhao, Z.; Baisley, T. L.; Leach, G. W. Molecular Orientation, Aggregation, and Order in Rhodamine Films at the Fused Silica/Air Interface. *J. Phys. Chem. B* **1999**, *103*, 1124−1133.
(66) Fedoseeva, M.; Letrun, R.; Vauthey, E. Excited-state dynamics of rhodamine 6G in aqueous solution and at the dodecane/water interface. *J. Phys. Chem. B* **2014**, *118*, 5184−5193.
(67) Novotny, L.; Hecht, B. *Principles of Nano-optics*; Cambridge University Press: Cambridge, UK, 2012.
(68) Akselrod, G. M.; Argyropoulos, C.; Hoang, T. B.; Ciracì, C.; Fang, C.; Huang, J.; Smith, D. R.; Mikkelsen, M. H. Probing the mechanisms of large Purcell enhancement in plasmonic nanoantennas. *Nat. Photonics* **2014**, *8*, 835−840.
(69) Campagnola, P. J.; Loew, L. M. Second-harmonic imaging microscopy for visualizing biomolecular arrays in cells, tissues and organisms. *Nat. Biotechnol.* **2003**, *21*, 1356−1360.
(70) Kenue, S. K. Lanelok: Detection of lane boundaries and vehicle tracking using image-processing techniques-part II: Template matching algorithms. *Proc. SPIE* **1989**, *1195*, 234−245.
(71) Prasanna, K.; Krishnan, V. Efficient parallel algorithms for image template matching on hypercube SIMD machines. *IEEE Trans. Pattern Anal. Mach. Intell.* **1989**, *11*, 665−669.
(72) Wagner, R.; Galiana, H. Evaluation of three template matching algorithms for registering images of the eye. *IEEE Trans. Biomed. Eng.* **1992**, *39*, 1313−1319.

DOI: 10.1021/acs.nanolett.9b02239
Nano Lett. 2019, 19, 6192−6202